Peptide template effects for the synthesis and catalytic application of Pd nanoparticle networks†

Anshuman Jakhmola, Rohit Bhandari, Dennis B. Pacardo and Marc R. Knecht*

Received 21st October 2009, Accepted 17th November 2009
First published as an Advance Article on the web 23rd December 2009
DOI: 10.1039/b922018f

Translation of nanomaterials from spherical to other shapes has demonstrated property and activity enhancement for applications ranging from optics to catalysis. Unfortunately, synthetic techniques for the controlled production of shaped nanomaterials, which can employ harsh conditions, remains challenging. In contrast, the fabrication of nanostructures using peptides has achieved the generation of functionally active materials using bio-conditions; however, these methods are typically limited to spherical materials. By merging these techniques, the biomimetic/ambient production of functional, shaped nanostructures may be achieved. Here we present the fabrication of non-spherical Pd nanostructures prepared using a peptide template. By controlling the Pd : peptide ratio, the production of at least three different Pd morphologies is possible: nanoparticles, short linear nanoribbons, and nanoparticle networks. Furthermore, all of the materials are active for Stille C-coupling catalysis using aqueous and room temperature conditions at low Pd concentrations. The results suggest that both the zerovalent Pd materials and the ligand surface structure modulate the reactivity, which may be exploitable for optimal functionality.

Introduction

Metal nanomaterials have gained considerable attention by the scientific community in the past decade due to their potential uses in a wide variety of multidisciplinary fields.[1–3] This interest is derived from the property enhancement that occurs due to their small size, either through strong optical properties or a maximization of the surface-to-volume ratio.[1,4] Much effort has been directed towards the fabrication of Pd nanostructures due to their desirable catalytic applications for such reactions as olefin hydrogenation and carbon bond formation.[1,5–10] A variety of strategies have been developed for the synthesis of Pd nanomaterials; however, the vast majority result in production of spherical particles whose surface is passivated by a dense monolayer of ligands.[11] While the size of the materials may be within the nanoregime, the full surface coverage by the ligands in these methods may disrupt or prevent catalytic reactivity *via* surface poisoning, which prevents the interactions of the reagents with the catalytic metal. Various shape-controlled syntheses have also been reported, resulting in production of Pd nanorods, nanobars, nanocubes, and triangular nanoplates.[5,10,12] These methods typically rely upon controlled faceted growth of the Pd nanomaterials from selected seeds in solution that display appropriate crystallographic defects. This shaped synthetic ability is of interest as some Pd catalytic reactions have been shown to be dependent upon the crystallographic face of the material.[9] Beyond catalysis, Pd nanomaterials have also been used as materials for H_2 storage.[13,14] This capacity arises in two manners: binding of the H-atoms within the crystalline lattice of the Pd itself to form Pd–H[13] or as a catalyst for H_2 spillover onto adsorbent materials.[14] While both techniques are viable H_2 storage mechanisms, a large catalytic Pd surface area is required to interact with H_2 molecules to cleave the H–H bond. Unfortunately, optimal materials remain a significant challenge for both H_2 storage and homo- and heterogeneous catalysis due to synthetic limitations to produce highly active Pd nanomaterials with optimization of both the exposed crystallographic facets and the ligand surface display. Such materials may be achieved by controlling the material shape and size to maximize the surface-to-volume ratio and the ligand set to mediate reagent interactions with the catalytic surface.

Nanoparticle networks (NPNs) are a unique set of non-spherical materials composed of linearly aggregated nanoparticles that are intermingled to form a weave-like pattern.[15–20] Typically, the diameter of the structures is on the order of <20 nm and the overall length of the network can extend to the μm scale. These materials can possess a high surface area for metallic materials,[18] owing to the networked structure, which is desirable for applications where surface interactions and reactions are required for activity.[9,15,16,18,20] Many literature reports have focused on synthetic strategies to produce Au NPNs,[17] but recently, a few reports have been published for the production of NPNs composed of Pt and Pd.[15,16,18–20] NPNs of these materials would be of interest for catalytic and energy applications as their high surface areas and controlled structures would be available for optimal interactions with reagents in solution.[15,20] These highly integrated materials are typically prepared using a soft template-based methodology.[15,16,18,20] For instance Pt NPNs have been produced using the surfactant cetyltrimethylammonium bromide, which, under precise conditions, forms wormlike micellular networks of the surfactant.[18] To this

Department of Chemistry, University of Kentucky, Lexington, KY 40506-0055, USA. E-mail: mrknec2@email.uky.edu
† Electronic supplementary information (ESI) available: Additional TEM images and control analyses. See DOI: 10.1039/b922018f

network, Pt^{2+} ions are added, from which they are able to complex to the ammonium headgroup within the scaffold that, upon reduction, results in controlled growth mechanisms to produce Pt NPNs. While this method produces Pt NPNs, adaptation of the system for the generation of Pd NPNs results in the fabrication of significantly altered materials with larger diameters and less controlled features. Similar pathways have been employed for the production of Pd NPNs using other polymeric templates. In this regard, polystyrene sulfonate is used as the template for the resultant networked structure.[20] These materials were found to be active electrocatalysts, suggesting that the metallic surface was solvent accessible to drive the reaction; however, highly basic reaction conditions are required for materials synthesis, which is a known synthetic hazard. To optimize NPN fabrication schemes, it would be desirable to employ bio-based methods, which could minimize the somewhat hazardous conditions of materials fabrication and use.

In consideration of the multitude of structures observed in nature, many researchers have focused on biomimetic methods for materials production.[2,21] This has resulted in an expansion in the field of biomineralization, to understand the complex interactions between biomacromolecules and inorganic composite materials, and its eventual adaptation to other materials-based processes. Unfortunately, while nature is quite diverse, it has not evolutionarily developed pathways for the production of all materials of technological interest. As a result, phage display techniques have been developed as a mechanism to isolate peptide sequences capable of fabricating non-natural materials[2,22–24] such as FePt,[25] ZnS,[23] Ag,[22] Pd,[8] $BaTiO_3$,[26] and TiO_2.[27] Additionally, adaptation of known biomineralization schemes for production of similar, but compositionally different materials are possible. For instance, Morse and coworkers have adapted the silicatein silicification enzymes of sponges to produce TiO_2[28] and GaOOH,[29] while the R5 silicification peptide of diatoms (SSKKSGSYSGSKGSKRRIL)[30,31] has demonstrated the ability to precipitate TiO_2[32] and TiP_2O_7.[33] Specifically, the R5 peptide is a unique target for materials production as its mode of action is dependent upon self-assembly in solution to produce peptide aggregates that display localized high concentrations of amines.[31,32] While this motif is required for metal oxide fabrication routes *via* catalytic polycondensation reactions, it also presents a locality for the sequestration of metal ions through amine binding, which could serve as a template for the fabrication of zerovalent materials. At present, little information is known about such techniques that may prove useful for the biomimetic fabrication of metallic materials.

Here we demonstrate the synthesis, characterization, and catalytic application of a variety of shaped Pd nanomaterials generated using the self-assembled R5 peptide as a bio-inspired template, as shown in Scheme 1. To that end, the amine moieties of the peptide sequester Pd^{2+} ions in a localized region that, upon reduction, coalesce within the peptidyl framework to grow into three differently shaped structures: spherical nanoparticles, short linear nanoribbons, and NPNs. The fabrication method is shown to be dependent upon the amount of Pd ions in the reaction such that below a critical threshold, only spherical Pd nanoparticles exist with diameters of ~3 nm; however, above this level, linear structures are prepared with widths of ~4 nm. The synthetic mechanism was probed using various Pd : peptide ratios during the fabrication procedure to understand the effects of Pd^{2+} concentration on the materials growth mechanism. The final materials were characterized using UV-vis spectroscopy, high-resolution transmission electron microscopy (HR-TEM), selected area electron diffraction (SAED), and powder X-ray diffraction (XRD). From these methods, it is evident that the final metallic materials are composed of zerovalent Pd and possess a polycrystalline structure that was achieved during the coalescence/aggregation formation mechanism. The materials are likely to be encapsulated within the peptide framework to impart their colloidal stability. Additionally, the catalytic activity of these materials was probed to determine any shape/framework effects for C–C bond formation in the Stille reaction. The catalytic results suggest that both the metallic surface area, as well as the depth of the metal nanomaterial within the peptide framework, act together to control the resultant functionality of the materials. These results are important for four key reasons. First, this study represents a synthetic understanding of strategies to attain shape directed Pd nanomaterials using peptide-based fabrication methods, which has proven to be challenging. Second, the structure of the final materials can be controlled by the ratio of Pd^{2+} to peptide used during the reaction, which allows for tuning of the product shape for desired functionalities. Third, materials syntheses for the R5 peptide have focused on spherical metal oxide fabrication; however, in the present study a route for shape-directed zerovalent metallic materials is

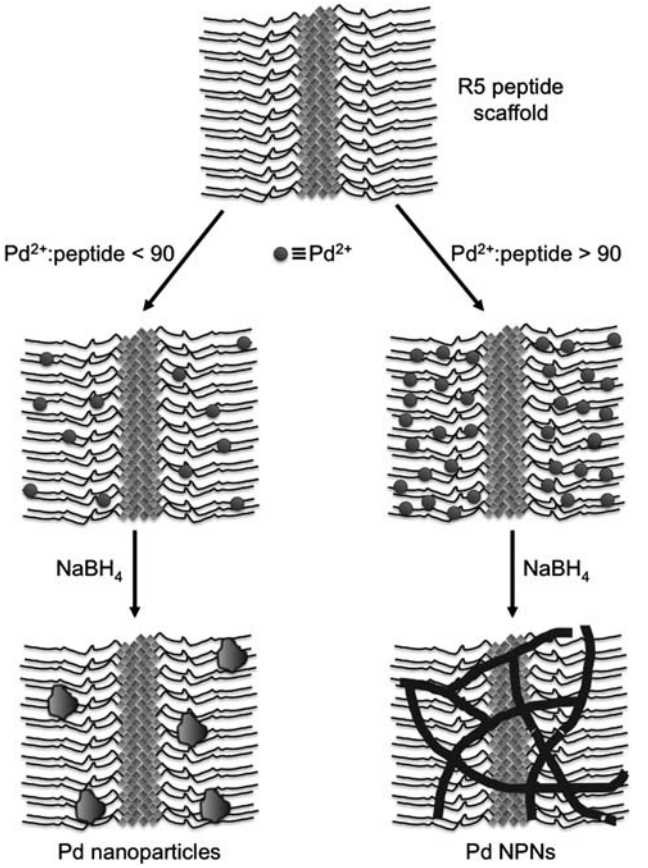

Scheme 1 Representative scheme for the synthesis of nanoparticles (left) or NPNs (right) employing a biomimetic template for materials growth.

obtained based on the assembled R5 scaffold. This suggests a high level of multifunctionality for this unique peptide sequence that could be exploited for a variety of metallic compositions. Fourth, the catalytic activities of the materials demonstrate that they are highly reactive under non-traditional, eco-friendly conditions. This indicates that the peptides on the surface diffusively interact with the inorganic component and thus allow for direct interactions with the reagents in solution. Together, such attributes are critical for the design and development of model catalysts that are compositionally similar, but structurally different, which could represent species for architectural design studies to elucidate optimally reactive structures.

Experimental

Chemicals

K_2PdCl_4 was purchased from Sigma-Aldrich, while $NaBH_4$ was purchased from EMD. FMOC protected amino acids and WANG resins for peptide synthesis were purchased from Advanced Chemtech (Louisville, KY). DMF, MeOH, and acetonitrile were acquired from Pharmco-Aaper. All chemicals were used as received. 18 MΩ cm water (Millipore; Bedford, MA) was used throughout.

Characterization

UV-vis analysis was conducted on an Agilent 8453 UV-vis spectrometer employing a 2.00 mm path length quartz cuvette (Starna). All spectra were background-subtracted against water, the solvent. HR-TEM images and SAED patterns were obtained using a JEOL 2010F transmission electron microscope operating at 200 kV with a resolution of 0.19 nm. All samples were prepared on 400 mesh carbon coated Cu grids (EM Sciences), where 5.00 μL of the reaction solution was pipetted onto the grid surface and allowed to dry in a desiccator. Powder XRD patterns were attained on a Bruker axis D8 discovery X-ray diffractometer with Cu Kα radiation at 1.5418 Å. The powder sample patterns were recorded by scanning the samples in a 2θ range of 20–90°.

Pd nanomaterial synthesis

Peptides were prepared using standard FMOC synthesis[34] and characterized by MALDI-TOF. For production of the metallic materials, 4.93 μL of an R5 stock solution (4.97 mM) was added to 3.00 mL of water. To this, 14.7, 22.1, 29.4, or 36.7 μL of a freshly prepared aqueous 100 mM K_2PdCl_4 solution was added, which represented a 60, 90, 120, or 150 fold excess, respectively, of Pd^{2+} to the peptide. After 15.0 min of vigorous stirring, reduction of the Pd^{2+}/peptide complex was achieved by adding 75.0 μL of a fresh 100 mM $NaBH_4$ solution to each reaction, which was further stirred for 1.00 h. The pH of each system was monitored and found to be ~6.8 ± 0.1 throughout the reaction, thus ensuring the stability of the peptide structure.[31] For catalytic studies and XRD characterization, the materials were dialyzed prior to analysis using cellulose dialysis tubing with a nominal molecular weight cutoff of 14 kDa against deionized water.

Catalytic Stille coupling

The C–C bond formation catalytic properties of the dialyzed Pd nanomaterials were tested for the Stille reaction by coupling 4-iodobenzoic acid and phenyltin trichloride to generate biphenylcarboxylic acid (BPCA) as the product. In a typical experiment, 0.50 mmol of 4-iodobenzoic acid (124 mg) and 0.60 mmol phenyltin trichloride (98.6 μL) were dissolved in 8.0 mL of 2.25 M aqueous KOH. To separate reactions, 0.50 mol%, 0.10 mol%, 0.05 mol%, 0.01 mol%, 0.005 mol%, and 0.001 mol% Pd were added based upon the concentration of Pd metal in solution. Such values varied for the three differently shaped Pd nanomaterials; therefore, a sufficient amount of water was added to reach identical volumes across all of the reactions. Each reaction was allowed to proceed for 24.0 h under constant stirring at room temperature. Once complete, the reactions were quenched by adding 50.0 mL of 5.0% aqueous HCl. The product was extracted three times with diethyl ether and the organic layers were collected and washed with a saturated NaCl solution. The ether layer was then dried with anhydrous Na_2SO_4 and 0.50 mmol 4-*tert*-butylphenol was added as an internal standard. The solvent was then removed using a rotary evaporator and ~1 mg of the solid mixture was redissolved in deuterated chloroform and characterized by ^1H NMR.

For analysis of the turnover frequency (TOF) and the reusability of the NPNs, the reaction was scaled up. For TOF analysis, this scale up allowed for aliquots to be extracted and quantitated to determine time dependent yields. The reaction was allowed to proceed for 5.0 h from which 4.0 mL aliquots were extracted and quantitated at 30.0 min time points using the standard procedure. Once all of the samples were quantitated, a plot of the mols product/mols Pd *versus* time was prepared from which the slope of the line represents the reaction TOF.

The reusability of the Pd NPNs was determined in the following manner. In a 20.0 mL vial, 0.375 mmol of 4-iodobenzoic acid and 0.45 mmol of phenyltin trichloride were dissolved in 6.0 mL of 2.25 M KOH. To this, 187.5 μL of the dialyzed Pd NPNs were added, which represents a catalyst loading of 0.05 mol% Pd. The reaction was allowed to proceed for 24 h with constant stirring at room temperature. After this time, a 2.0 mL aliquot of the reaction mixture was extracted and the product yield was quantitated. To the remaining 4.0 mL of the initial reaction, 0.25 mmol of 4-iodobenzoic acid and 0.30 mmol of phenyltin trichloride were added. The reaction was allowed to proceed for another 24.0 h after which a second 2.0 mL aliquot was removed and the product yield was quantitated. To the remaining 2.0 mL of the initial reaction, 0.125 mmol of 4-iodobenzoic acid and 0.15 mmol of phenyltin trichloride, were added and the reaction was allowed to proceed for another 24 h. After this final time point, the reaction was quenched and quantitated using standard methods. Throughout the duration of the experiment, the catalyst loading was maintained at 0.05 mol% Pd with respect to the amount of aryl halide in solution.

Results and discussion

To study the ability of the R5 peptide framework for the production of zerovalent Pd nanomaterials, different Pd : peptide

ratios were employed ranging from 60 to 150. To that end, the ratio was varied over four different values of 60, 90, 120, and 150, while the concentrations of the other reagents used in the synthesis remained constant. Upon reduction, the formation of zerovalent Pd nanostructures is anticipated due to the formation of a deep brown solution that remained stable over time. Based upon previous template synthetic schemes,[15,19,35] different nanostructures are anticipated at lower *versus* higher Pd^{2+} loadings of the peptide framework from spherical nanoparticles to NPNs, as shown in Scheme 1. This is controlled by the nucleation, growth, and assembly rates within the peptide scaffold (*vide infra*).

Fig. 1a presents an image of the solutions prepared at the four ratios studied after BH_4^- reduction. Samples prepared with a ratio of ≤120 produced stable brown solutions that possessed increasing degrees of color intensity that were proportional to the Pd : peptide ratio, as expected. Due to the solution stability of these materials, this suggests that the interactions between the zerovalent metal and the peptide scaffold are sufficiently strong enough to prevent bulk materials aggregation and that all of the Pd^{2+} was successfully loaded within the scaffold. For the highest ratio studied, 150, a black precipitate was observed within 15.0 min of reductant addition. This indicates that the peptide template has been saturated with the Pd^{2+} ions, and that extraneous ions remain in solution, thus resulting in bulk precipitation after reductant addition. Due to the lack of stability and the formation of Pd black, analysis of samples using ratios ≥150 were not studied.

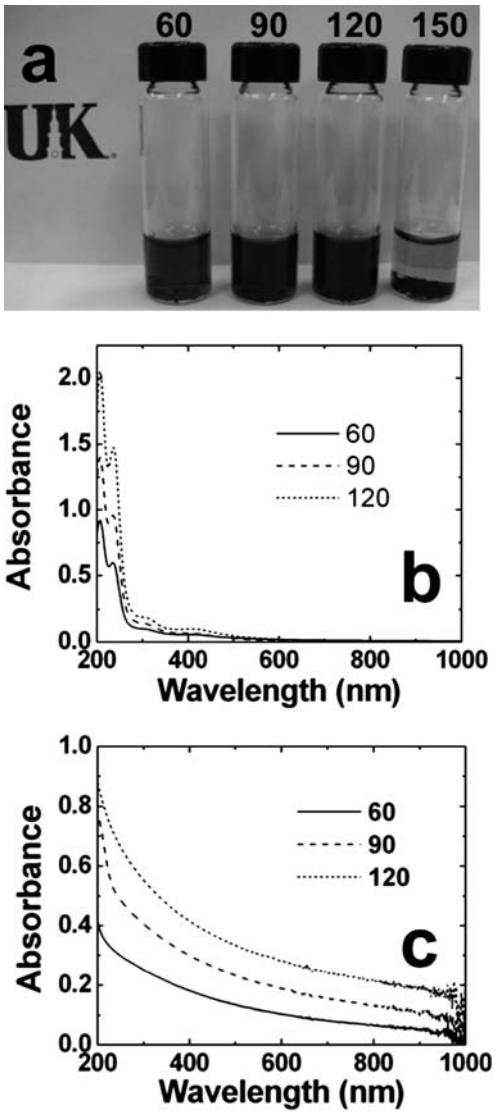

Fig. 1 Effects of template loading at various Pd : peptide ratios. Part (a) is an image of the reaction after $NaBH_4$ reduction. Note that the largest ratio resulted in materials precipitation. Parts (b) and (c) present the UV-vis analysis of the materials before and after reduction, respectively. The solid spectrum corresponds to a ratio of 60, the dash spectrum is for a ratio of 90, and the dot spectrum represents a ratio of 120.

Initial analysis of the materials was conducted using UV-vis spectroscopy. Fig. 1b presents the UV-vis spectrum of each of the materials prior to reduction. The solid spectrum represents the Pd^{2+}-peptide complex, prepared using a Pd : peptide ratio of 60. This analysis displays a peak at 228 nm corresponding to the ligand to metal charge transfer (LMCT) band for Pd^{2+}–peptide binding, which occurs *via* the amine moieties of the sequence.[35,36] Additionally, small absorbances at ~300 and 430 nm arise from the $PdCl_4^{2-}$.[36] For the higher ratios studied, 90 (dash spectrum) and 120 (dot spectrum), identical spectra are observed; however, the intensity of the LMCT band increases with higher ratios as expected. UV-vis analysis of the materials after reduction is presented in Fig. 1c. Each sample demonstrates a featureless spectrum with an exponential increase in absorbance as the wavelength decreases, as is typical for Pd nanomaterials.[37] Additionally, an increase in the absorbance intensity between the individual samples at all wavelengths is observed as the Pd : peptide ratio increases such that the absorbance for the 60 sample (solid spectrum) is less than the 90 sample (dash spectrum), which is less than the 120 sample (dot spectrum). This absorbance change is likely attributable to the formation of larger sized structures at higher Pd : peptide ratios, which would increase the absorptivity and scattering of the materials in solution.[37]

To determine the effects of the variations in the Pd : peptide ratio, TEM and powder XRD analyses were conducted, as shown in Fig. 2. Characterization of the samples 1.0 h post reduction by TEM demonstrated a shift in particle morphology that was able to be resolved using low-resolution TEM imaging. Analysis of the sample with a loading of 60 Pd-ions per peptide (Fig. 2a) demonstrated the formation of spherical Pd nanoparticles; however, when the ratio was increased to 90 (Fig. 2b), the formation of short strand-like metallic nanoribbons was observed. This elongation effect was further evident when the ratio was increased to 120 (Fig. 2c) where branched, Pd NPNs are observed in the sample. Note that for Pd : peptide ratios >120, materials precipitation was noted. From the observed structural changes, this suggests that a specific growth mechanism controls the morphology of the final structure such that higher loading of Pd-ions within the soft template results in the formation of the linearized branched structures.

Fig. 2d presents the powder XRD analysis of the materials post dialysis. Each sample, regardless of the amount of Pd in the system, demonstrated identical reflections associated with the face-centered cubic (*fcc*) structure of Pd metal. For this analysis,

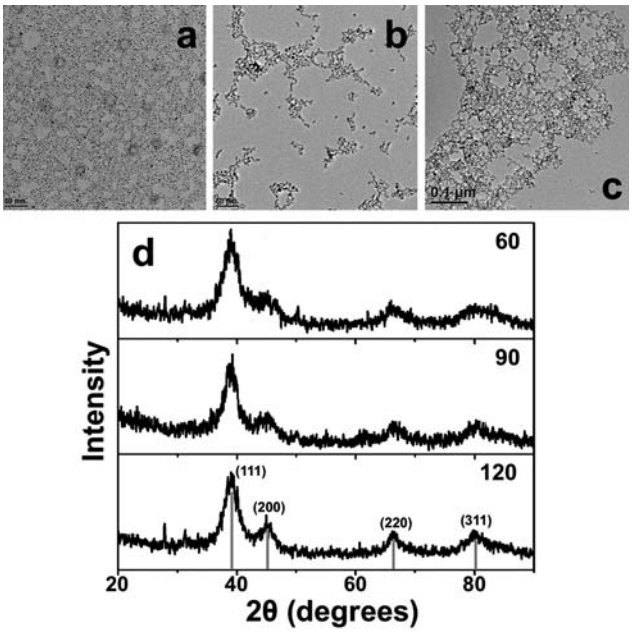

Fig. 2 TEM images of the materials using a Pd : peptide ratio of (a) 60, (b) 90, and (c) 120. Part (d) presents the XRD analysis of the materials after dialysis. All samples demonstrate diffraction patterns consistent with Pd.

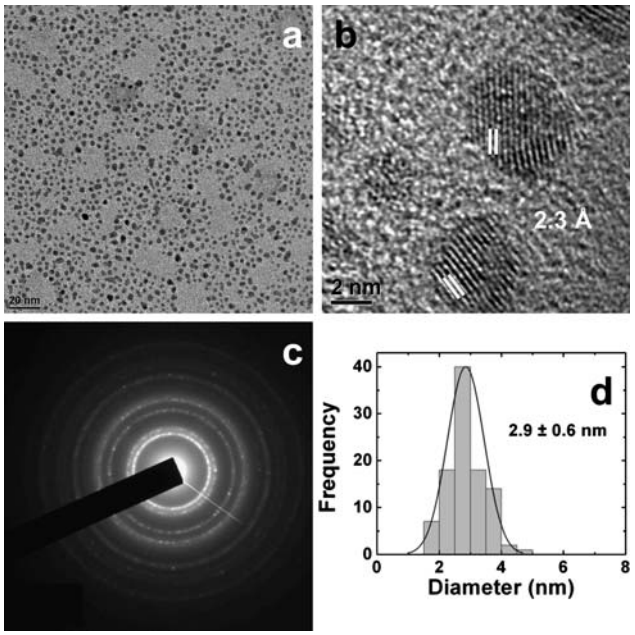

Fig. 3 Characterization of the structures prepared using a ratio of 60. Part (a) is a low resolution TEM image, while part (b) presents an HR-TEM image of the materials. Part (c) is the SAED ring pattern of the sample and part (d) is the sizing analysis of the diameter of the materials.

diffraction peaks were indexed to the (111), (200), (220), and (311) reflections of the zerovalent metal. The peaks were also observed to be somewhat broad. For each sample, the full width at half height value decreased for increasing Pd loadings, with the sample prepared with a Pd : peptide ratio of 60 having the broadest peak while the 120 sample has the narrowest peak. Such changes are likely attributable to the small particle size of the materials on the nanoscale. Scherrer's analysis of the peak at $39°2\theta$ indicates particle dimensions of 2.7 nm, 3.4 nm, and 4.2 nm for the 60, 90, and 120 samples, respectively, which is consistent with the observed changes in peak widths.

Further, high-resolution TEM analysis of the materials was conducted to fully characterize the structures and the effect of template loading. Fig. 3 presents this analysis for the sample with a loading of 60 Pd^{2+}-ions per peptide. Specifically, Fig. 3a shows the synthesized Pd nanoparticles, which are highly dispersed along the TEM grid surface. Analysis of a random selection of 100 nanoparticles indicates that the materials possess a diameter of 2.9 ± 0.6 nm, as presented in the histogram of Fig. 3d. This experimentally derived size is based upon multiple TEM images from the grid surface and is consistent with the value attained by Scherrer's analysis of the powder XRD pattern (2.7 nm) within the error of the study. Based upon theoretical calculations, spherical Pd nanoparticles of this size would contain ~825 Pd atoms assuming an empirical atomic radius of 140 pm for a single Pd atom.[8] HR-TEM analysis of two of the Pd nanoparticles prepared from the sample is presented in Fig. 3b. Clear lattice fringes are observed from these nanoparticles with a d-spacing of 2.3 Å, which fits with the d-spacing of the (111) plane of *fcc* Pd. Finally, the SAED pattern of an individual particle, presented in Fig. 3c, possesses diffraction rings associated with the (111), (200), (220), (311), (222), and (400) atomic planes of Pd. This analysis is fully consistent with the powder XRD results of Fig. 2d indicating the production of *fcc* spherical Pd nanoparticles under these synthetic conditions.

Fig. 4 presents the analysis for the materials prepared employing the Pd : peptide ratio of 90. TEM imaging of these

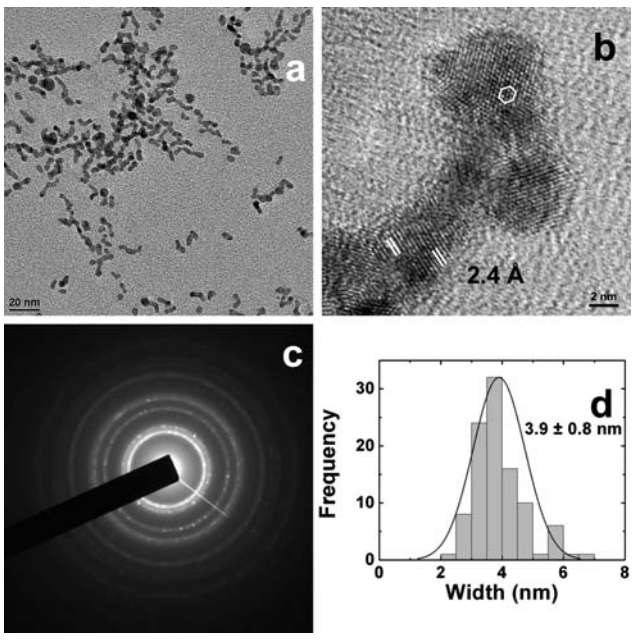

Fig. 4 Characterization of the structures prepared using a ratio of 90. Part (a) is a low resolution TEM image, while part (b) presents an HR-TEM image of the materials. Part (c) is the SAED ring pattern of the sample and part (d) is the sizing analysis of the width of the materials.

materials, Fig. 4a, indicated that ribbon-like nanostructures were prepared using these reaction conditions. This is in stark contrast to the spherical nanoparticles fabricated using the lower ratio of 60. The short, one-dimensional materials were linear in nature and occasionally presented structures that were branched to form a Y-type intersection. Additionally, the final materials were observed to be bent and possess bulging points, which may arise from the growth mechanism. Sizing analysis of the average width of these materials is shown in Fig. 4d, which indicates a value of 3.9 ± 0.8 nm. This value was attained at a clearly distinct region of the ribbon-like structure to avoid complications of overlapping materials. Interestingly, this value corresponds quite well with the Scherrer's analysis value of 3.4 nm attained from the XRD analysis. HR-TEM characterization of these one-dimensional structures is presented in Fig. 4b. From this image, it is clear that the materials are polycrystalline, which is likely evidence of an aggregation process between two initially separated nanostructures. Hexagonal close packing of the Pd atoms is observed in the HR-TEM image of the materials and is denoted in the figure. In addition, fringes of the Pd (111) lattice are observed with a d-spacing of 2.4 Å. Finally, the SAED pattern obtained from a region of a single species in this sample is consistent with those attained for the 60 sample shown above and the *fcc* crystalline structure of Pd (Fig. 4c).

Characterization of the final sample studied, with a ratio of 120 Pd^{2+} ions per peptide, demonstrated the formation of Pd NPNs, as shown in Fig. 5a. In this network of zerovalent Pd nanomaterials, a highly bifurcated mesh-like structure is observed, which is noted to be significantly more integrated as compared to the previously described one-dimensional ribbon-like structures of the 90 sample. The Pd NPNs possessed a width of 4.1 ± 1.2 nm (Fig. 5d), which is consistent the Scherrer's analysis above (4.2 nm). HR-TEM analysis of the materials, presented in Fig. 5b, demonstrated that the materials are polycrystalline in nature with Pd (111) lattice fringes of 2.3 Å, which has been observed for all samples studied in the present analysis. Additionally, in the HR-TEM image, it is evident where branching points exist within the structure from which subsequent elongation and growth can occur to generate the mesh-like characteristic of the Pd NPNs. For instance, both circular bulges and linear regimes are observed that likely arise during the growth phase of the materials *via* controlled particle assembly/aggregation. Finally, SAED characterization of the materials, displayed in Fig. 5c, is fully consistent with all of the zerovalent Pd materials produced.

Changes to the nanomaterials' shape over traditional spherical particles can result in activity and surface area enhancements; however, for these effects to be technologically useful, the structures must remain stable in solution over time without changing morphologies. To determine the stability of the bio-inspired Pd NPNs, the following TEM analysis was conducted. Immediately after reductant addition, a TEM sample was prepared of the reduced materials. The reaction was then vigorously stirred for 24.0 h in air, from which a second sample was prepared. TEM analysis of these samples was then conducted and is presented in Fig. 6. For the 0.0 h time point, Fig. 6a and b, Pd NPNs are observed. The bifurcated structure is highly homologous and can extend for μm lengths, while maintaining their widths on the order of 4 nm. For the 24.0 h time point, Fig. 6c and d, highly similar structures were observed as compared to those attained immediately after reduction. The NPNs remained structurally intact after 24.0 h while stirring under ambient conditions. The insert of Fig. 6d presents the SAED pattern of the materials 24.0 h post reduction, which is

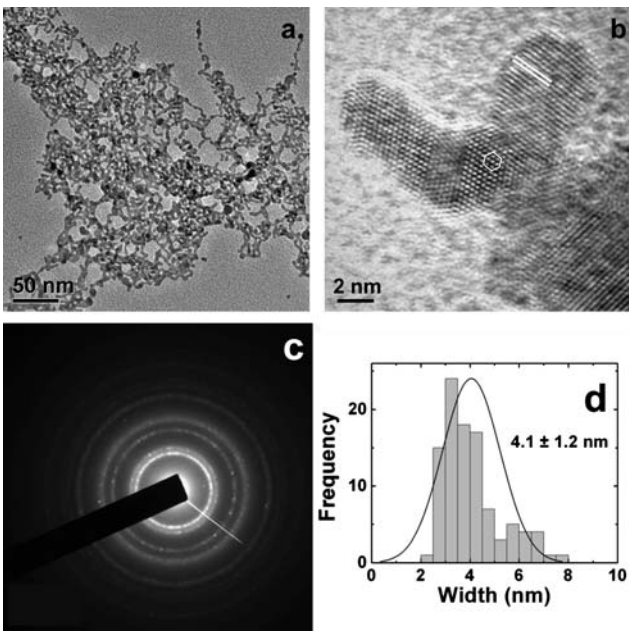

Fig. 5 Characterization of the structures prepared using a ratio of 120. Part (a) is a low resolution TEM image, while part (b) presents an HR-TEM image of the materials. Part (c) is the SAED ring pattern of the sample and part (d) is the sizing analysis of the width of the materials.

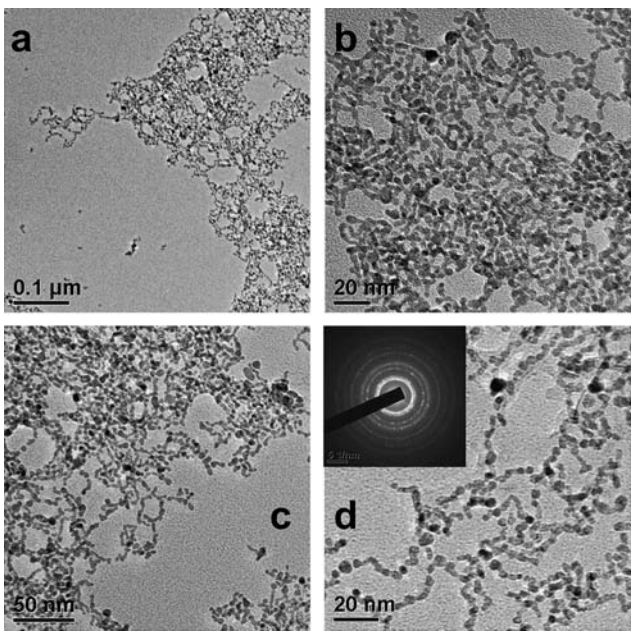

Fig. 6 TEM analysis of NPN stability. Parts (a and b) represent the materials attained immediately after reduction, while parts (c and d) display the materials attained 24.0 h after reduction. The insert of part (d) presents the SAED pattern of the materials and is consistent with *fcc* Pd.

fully consistent with zerovalent, *fcc* Pd. Together, this suggests that the integrated structures may be maintained over time while possibly being difficult to oxidize, which can adversely affect their reactivity. Furthermore, the materials did not precipitate after two months at room temperature on the benchtop.

Based upon the results presented above, a more resolved image of the synthetic mechanism for the peptide-based formation of non-spherical Pd nanomaterials could be described. Such a level of understanding is important for biomimetic materials fabrication and their adaptation to synthetic schemes for the generation of higher-ordered shaped nanostructures. The synthetic process is based upon the self-assembled scaffold of the R5 peptide in solution. The collective organization of the peptides in three-dimensions acts as a soft template that presents a region of localized high amine concentrations, which can bind and sequester the Pd^{2+} ions within the organic framework. At all ratios of Pd : peptide, immediately after metal-ion reduction, nucleation and growth of individual Pd nanoparticles occurs. At the lowest metal loading (60), the Pd-ions are likely to be highly dispersed within the framework, that upon reduction begin to form nuclei at distinct locations within the template. Based upon this condition, the nucleation sites are likely to be sufficiently spaced within the framework such that the interparticle distance is maximized to prevent interactions between individual nanoparticles that would lead to their aggregation. Particle growth continues in solution until the source of Pd is exhausted to produce the final sized particles. This results in individual particles interspersed throughout the assembled R5 peptide scaffold.

As the Pd loading in the reaction is increased, a larger number of nucleation sites develop within the template during BH_4^- reduction. Due to this effect, the distance between individual nanoparticles decreases to within appropriate limits to allow for aggregation between multiple particles in the peptide structure. As these particles begin to aggregate, they do so in a manner that results in their linear elongation, rather than through formation of increasingly larger particles. This elongation effect is possibly due to the strands of the peptide template that may sterically drive directional growth based upon the orientation of the nanoparticles before the coalescence event and their interactions with the functional groups of the peptide. To that end, the peptide strands of the template control the orientation of the aggregating particles and their specific approach, thus resulting in the linearized structures; however, metallic branching points can arise from aggregation of particles approaching from multiple directions at a single focal point. Furthermore, the direction of assembly may possibly be controlled by the metallic surface coverage of the Pd nanoparticles by the peptide, which could result in exposed metal regions on the closely spaced particles that would act as aggregation/assembly points.

For the largest level of template loadings by the metal ions (120), highly bifurcated Pd NPNs are observed. This is a further extension of the elongation process that arises from the larger loading of Pd into the peptide scaffold. Under these conditions, nucleation and growth of a larger quantity of nanoparticles occurs within the template, as compared to the lower ratios. From this quality, more extensive assembly/aggregation can occur, employing the directional method associated with the peptide stands of the template, thus resulting in the mesh-like NPN structure. Since the quantity of particles per template scaffold is so high, multiple aggregation points occur from the specific particle density. Additionally, at this ratio, the Pd loading is still under a critical threshold from which bulk materials production occurs; such an event is anticipated when excessive Pd^{2+} is added to the system that cannot be sequestered by the peptide scaffold. Indeed, when a ratio of 150 Pd-ions to peptide was employed, precipitation of Pd black materials rapidly results, thus suggesting that at the lower values, the Pd-ions are fully loaded within the R5 template.

To probe the reaction mechanism, a set of specific control studies was completed. In the first analysis, K_2PdCl_4 was reduced in the absence of the R5 peptide at the reaction concentrations employed for the 60, 90, and 120 samples. As shown in the ESI,† Figure S4a, for all three cases, bulk Pd metal precipitated as no surface passivant was present in solution. In the second control, to probe the effects of the peptide template for materials production, the R5 peptide was replaced with the non-assembling A3 peptide (H_2N-AYSSGAPPMPPF-COOH) that is specific for Au and Ag.[22,38] In this analysis, presented in Figure S4b of the ESI,† a black precipitate was again observed for all three ratios. Furthermore, when the Pd-specific Pd4 peptide was used, spherical particles are achieved due to the binding effects of the peptide sequence directly onto the nanoparticle surface.[8,39] Interestingly, Pd : peptide ratios of <4 must be used with the Pd4 peptide to prepare the spherical particles due to materials precipitation at higher loadings. These control studies suggest that the R5 framework does indeed act as a template to mediate NPN formation.

Based upon the composition and structures of the three materials produced, all of which are contained within a peptide scaffold, catalytic activity may be possible for a variety of reactions including C-coupling[1,6–8,40] and olefin hydrogenation.[9] With the diffuse peptide framework, it is possible that the catalytic reagents can penetrate the surface, interact with the metallic species to generate products, and these products can then diffuse out into the aqueous medium. From the different metallic nanostructures, changes in activity may arise from the different shapes of the materials and their position within the peptide framework, which are known to alter nanoparticle reactivity.[9,41] To test their catalytic potential, each of the three sets of Pd nanostructures were employed as catalysts for Stille coupling[40] between 4-iodobenzoic acid and phenyltin trichloride to produce biphenylcarboxylic acid (BPCA), as shown in Fig. 7a. Identical reaction conditions were used, as described in the experimental section; therefore comparison between their reactivities can be drawn and possibly related to their individual structure. Note that these reaction conditions employ water as the solvent and operate at room temperature.

Initial analysis for all three materials with a catalyst loading of 0.500 mol% Pd in the reaction demonstrated quantitative production of BPCA within 24.0 h. Catalyst loadings are based upon the total concentration of Pd in solution and not the concentration of Pd nanostructures or surface metal atoms as is consistent with previous studies.[6,7] By using the absolute Pd concentration, a more representative analysis can be conducted as the exact mechanism by which C-coupling reactions employing Pd nanoparticles proceeds is unclear. With positive confirmation of the catalytic abilities, a loading analysis was conducted

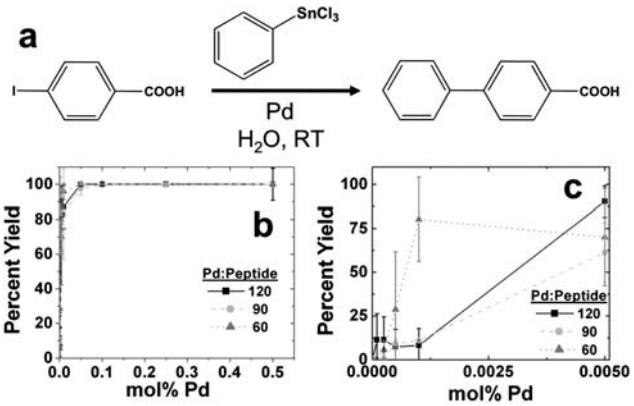

Fig. 7 Catalytic loading analysis for the Pd nanomaterials. Part (a) presents the model Stille coupling reaction. Part (b) displays the product percent yield as a function of catalyst loading, while part (c) presents an expanded analysis of the lower catalyst concentration region.

to determine the minimum catalyst loading required to achieve quantitative yields under these conditions. Such studies are important to minimize the amount of precious metal catalyst required and its possible eventual loss. Fig. 7b and c present these results for all three prepared samples, 60, 90, and 120, that demonstrate a high degree of reactivity from quite low catalyst concentrations. For the spherical particles prepared using 60 equiv. of Pd, a product yield of ≥75% was achieved at catalyst loadings of 0.001 and 0.005 mol%; however, at higher Pd loadings, 100% quantitative yields were achieved. For the 1D linear nanoribbons fabricated with 90 equiv. of Pd, noticeable product formation was not evident until 0.005 mol% Pd, where 55% product yields were achieved. At progressively higher catalysts loadings, quantitative product yields were also obtained for the 90 species. Using the Pd NPNs, nearly identical results were achieved as compared to the other 1D structures; 80% product yields were obtained at 0.005 mol% Pd with quantitative yields at higher catalyst loadings. Such results suggest different catalytic capabilities based upon the metallic nanomaterial structure, which can be tuned at the synthetic level. It is also interesting to note that the materials maintained their high levels of activity at low loadings even after stirring in air for multiple days. Pd nanomaterials are easily oxidized under such conditions; therefore, this stability may prove useful for future reaction designs.

The turnover frequency (TOF) for each of the three systems was additionally determined. Each value represents an average across triplicate reactions to determine the reproducibility of the analysis. For this study, the reaction was scaled up by five fold, from which aliquots can be taken and quantitated to monitor the progression of the reaction. The results for all three samples are presented in Fig. 8. The individual catalytic system data, shown in Fig. 8a for the 60, 90, and 120 samples, is plotted as the mol BPCA/mol Pd as a function of time in hours. The slope of the line thus represents the TOF value. A comparison of the three individual results is displayed in Fig. 8b. For each system, the observed TOFs were surprisingly close in value with the 60 sample possessing a TOF of 452.4 ± 16.4 mol BPCA (mol Pd × h)$^{-1}$, while the 90 and 120 systems demonstrated TOF values of 334.3 ± 38.3 mol BPCA (mol Pd × h)$^{-1}$ and 437.1 ± 14.3 mol BPCA (mol Pd × h)$^{-1}$, respectively. Statistical analysis of the

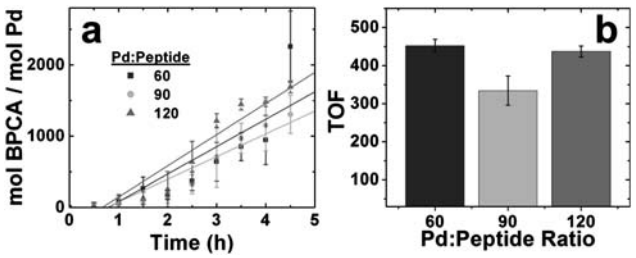

Fig. 8 TOF analysis of the nanomaterials. Part (a) presents the TOF data for the three structures, while part (b) presents the TOF comparison (y-axis units = mol BPCA (mol Pd × h)$^{-1}$).

three average TOFs employing a standard t-test indicates that the 60 and 90 values, as well as the 90 and 120 values, are different at the 98% confidence level. Comparison of the 60 and 120 samples indicates no statistical difference. It is important to remember that while the TOFs may be different, they still reach 100% yields in <24.0 h; therefore, each system is capable of achieving high product yields, which is a highly desirable attribute. Additionally, each TOF analysis was conducted at 0.050 mol% Pd calculated based upon the concentration of Pd in solution.[6,7] As such, each sample is normalized with respect to one another based upon the Pd concentration to remove any effects of the Pd atom concentrations.

To further study the catalytic properties of the Pd NPNs prepared from the 120 Pd : peptide system, the ability for the materials to be used in multiple reactions was studied. For this analysis, a series of aliquot quantitation with subsequent reagent additions to the initial reaction mixture was used as is consistent with previous studies.[5,7] In this sense, the catalyst loading was maintained at 0.05 mol% and no Pd was lost during product extraction and reaction workup. This effect was of significant concern due to the ultra-low concentration of catalyst in solution. From this analysis, the catalyst was studied after three reactions for the formation of the model BPCA compound with 100% product yields determined after each step. Such abilities suggests that the materials are highly active and can be repeatedly used in reaction schemes to avoid loss of the precious metal catalyst over time.

The different TOF values and product yields at the lowest concentrations of catalyst are likely the effect of the nanomaterial structure, which controls the resultant catalytic functionality.[41] For each structure, the metallic nanomaterials are contained within the peptide framework. Should the zerovalent metal be exposed to solution outside of the protective peptide scaffold, bulk aggregation would likely be prevalent as exposed metallic surfaces from multiple structures would eventually aggregate and precipitate from solution. The materials prepared at Pd : peptide ratios of ≤120 were stable in solution for extended periods of time, which suggests that the metallic species do not extend beyond the peptide boundaries. Furthermore, when considering this general structural motif, it is evident that two specific changes are likely to occur based upon the size and shape of the metallic component. First, the metallic surface area for the individual samples changes based upon the nanomaterial shape. This effect can alter the number/degree of interactions between the reagents and the metal catalyst. Second, the distribution of the depth of the metallic materials within the peptide scaffold will

vary between samples with differing metal-ion loadings during the synthetic procedure. For instance, at the lower loadings, less metal is available per peptide framework; therefore, a lower amount/number of zerovalent Pd nanomaterials are prepared within the individual peptide template, which can be buried deep within the structure. However, as the loading amount of Pd increases, the 1D Pd NPNs will consume an extensive amount of space within the scaffold, thus pushing Pd^0 metal closer to the surface of the framework. As such, the starting materials for the C-coupling reactions would have to penetrate deeper within the peptide template to interact with the spherical particles (60 sample), whereas, with the Pd NPNs (120 sample), the reagent penetration depth would be significantly lowered to where the reagents and final products can diffuse in and out of the system quicker. Such diffusion effects have previously been shown to modulate catalytic activity for similar template-based materials.[41]

For the present biomimetic systems, the differing catalytic results are likely to be a combination of the two above described effects. It is important to remember that the actual amount of Pd in solution for each reaction is identical, regardless of nanoparticle shape or peptide template loading; therefore, the observed changes in catalytic reactivity are not the result of differing amounts of Pd metal in the reaction mixture. Furthermore, attempts were made to quantitate the surface area of the materials; however, the mass of the sample required for this analysis proved to be prohibitory. For the 60 sample that produces individual Pd nanoparticles, it is anticipated that the surface area of Pd in solution would be the greatest. Unfortunately, these particles are diffused throughout the framework and can be buried close to the core of the structure. While the surface area is likely the highest in this system, the diffusability to and from the catalytically reactive surface by the reagents and products is the most difficult, which could slow the reaction progression.[41] As the shape of the materials changes from zero-dimensional to one-dimensional linear structures, it is anticipated that the surface area of the system would decrease, which would likely decrease the reaction rate; however, since the peptide template size is the same across all three different materials, it is envisioned that the metallic materials could be closer to the surface of the framework with higher metal loading values. As a result, the reagent pathway to reach the surface is significantly reduced to allow for a quick efflux of the reagents and products for a more rapid reaction rate. Similar results have recently been reported for the non-specific enzymatic production of metal oxides where the active site depth within the enzyme structure plays a role in its ability to produce the oxide-based materials.[42] This effect would enhance the reactivity for the NPNs, which contain the highest Pd : peptide ratio. While one of these two factors, surface area and amount of Pd per template, are maximized for the 60 and 120 materials, respectively, they are both likely to be minimized for the 90 sample at the intermediate loading. This should cause a decrease in the active surface area, as compared to the spherical nanoparticles, and a decrease in the reagent/product efflux rate due to reagent penetration depth as compared to the NPNs. As a result, decreased TOF values would be anticipated for the 90, Pd nanoribbons, which is observed in Fig. 8b. This diffusion process also likely results in the observed sigmoidal-like nature of the TOF analysis presented in Fig. 8a. At present, we are unaware of any method to deconvolute the diffusion process from the catalytic reactivity. Additionally, as discussed below, the reaction mechanism is unclear. Collectively, these effects are likely to give rise to the sigmoidal curves, which fitting *via* a linear regression is anticipated to average these effects to achieve a degree of quantitative data to compare the materials reactivity.

Comparison of the TOF values to other nanomaterials for Stille coupling demonstrate different reaction rates. For instance, Garcia-Martinez *et al.* have reported a TOF of ~2000 mol product/(mol Pd × h)$^{-1}$ for Pd nanoparticles with an average diamater of 1.7 nm encapsulated within a dendrimer host.[7] Additionally, we have recently described the Stille coupling application of Pd nanoparticles prepared using a Pd specific peptide.[8] In that study, 1.9 nm particles are prepared with the peptide bound directly to the surface. Employing these materials, a TOF value of ~3200 mol product (mol Pd × h)$^{-1}$ was determined.[8] For both of these systems, the higher values likely arise from the larger surface area and enhanced surface-to-volume ratio, as compared to the spherical 60 sample, which has a larger particle diameter (~2.9 nm). Astruc and coworkers have employed Pd nanoparticles of ≤2.8 nm, again prepared in a dendrimer template, for Suzuki coupling, which substitutes a boron compound for the tin complex of Stille coupling.[6] In this reaction, TOF values of <375 mol product (mol Pd × h)$^{-1}$ were reported that are equal to or smaller than those observed for the present materials. Furthermore, Chen *et al.* have recently reported a TOF value of 14.2 mol product (mol Pd × h)$^{-1}$ for Suzuki coupling employing Pd nanorods,[5] which is lower than the values reported here for the linear NPNs. This suggests that the peptide templated Pd NPNs demonstrate significant reactivity, as compared to comparable materials, and may represent unique structures to model nanomaterial catalytic reactivity.

Finally, it is important to note that the actual reaction mechanism for C-coupling reactions employing nanoparticles is only partially understood. Two competing mechanisms exist that describe either (1) the reaction occurring at the nanoparticle surface, or (2) Pd atoms are leached from the materials from which the reaction is driven by the released atoms.[1] We have attempted to view any structural changes to the Pd materials presently studied, but by operating at atomic Pd concentrations of <62.5 μM (0.1 mol% Pd), which would be substantially lowered when considering the concentration of nanomaterials, the ability to isolate and study structures by TEM post-reaction is rather difficult. From this analysis after the catalytic reaction, we were unable to observe any materials; however, further studies are being conducted in this area. Nevertheless, both mechanisms are dependent upon Pd surface area, whether to drive the reaction at the surface or to extract metal atoms in a quick efficient manner; therefore, the amount of surface area present is a critical factor for the reactivity.

Conclusions

In conclusion, by using a self-assembling peptide template, we have been able to prepare different shapes of Pd nanostructures. The shape control is gained at the stoichiometric level, which employs the peptide framework as a template to bind Pd^{2+} and direct the growth of the materials. As such, the peptides act as a template, which results in the production of spherical,

linear/ribbon-like, or NPNs of Pd when a Pd : peptide ratio of 60, 90, or 120, respectively, is employed. Additionally, the catalytic capabilities for each of the three systems were analyzed for C-coupling *via* the Stille reaction using a water based solvent at room temperature. Such conditions were employed due to the biologically-based structures of the materials. The catalytic results suggest that the individual system reactivities are controlled by two specific factors: the metallic surface area and the proximity of the metal to the surface of the peptide framework. These results are important in determining structure/function relationships for nanocatalysts and can be used as model systems to elucidate attractive structure attributes to achieve new and enhanced catalysts. Furthermore, the diffused peptide framework encapsulating the Pd nanostructures may prove useful in the development of selective catalysts that employ the biomimetic scaffold as a gate. Such studies are presently underway in our laboratories.

Acknowledgements

Acknowledgment is made to the Donors of the American Chemical Society Petroleum Research Fund for partial support of this research with further support from the University of Kentucky also acknowledged. We thank L. Jackson and Dr B. C. Lynn for MALDI-TOF characterization of the synthesized peptides.

References

1 D. Astruc, *Inorg. Chem.*, 2007, **46**, 1884–1894.
2 M. B. Dickerson, K. H. Sandhage and R. R. Naik, *Chem. Rev.*, 2008, **108**, 4935–3978.
3 P. K. Jain, X. Huang, I. H. El-Sayed and M. A. El-Sayed, *Acc. Chem. Res.*, 2008, **41**, 1578–1586; C. J. Murphy, A. M. Gole, J. W. Stone, P. N. Sisco, A. M. Alkilany, E. C. Goldsmith and S. C. Baxter, *Acc. Chem. Res.*, 2008, **41**, 1721–1730; N. L. Rosi and C. A. Mirkin, *Chem. Rev.*, 2005, **105**, 1547–1562; M. R. Knecht and M. Sethi, *Anal. Bioanal. Chem.*, 2009, **394**, 33–46.
4 M.-C. Daniel and D. Astruc, *Chem. Rev.*, 2004, **104**, 293–346; P. K. Jain, S. Eustis and M. A. El-Sayed, *J. Phys. Chem. B*, 2006, **110**, 18243–18253.
5 Y.-H. Chen, H.-H. Hung and M. W. Huang, *J. Am. Chem. Soc.*, 2009, **131**, 9114–9121.
6 A. K. Diallo, C. Ornelas, L. Salmon, J. R. Aranzaes and D. Astruc, *Angew. Chem., Int. Ed.*, 2007, **46**, 8644–8648.
7 J. C. Garcia-Martinez, R. Lezutekong and R. M. Crooks, *J. Am. Chem. Soc.*, 2005, **127**, 5097–5103.
8 D. B. Pacardo, M. Sethi, S. E. Jones, R. R. Naik and M. R. Knecht, *ACS Nano*, 2009, **3**, 1288–1296.
9 O. M. Wilson, M. R. Knecht, J. C. Garcia-Martinez and R. M. Crooks, *J. Am. Chem. Soc.*, 2006, **128**, 4510–4511.
10 Y. Xiong, H. Cai, B. J. Wiley, J. Wang, M. J. Kim and Y. Xia, *J. Am. Chem. Soc.*, 2007, **129**, 3665–3675.
11 D. Ghosh and S. Chen, *J. Mater. Chem.*, 2008, **18**, 755–762; F. P. Zamborini, S. M. Gross and R. W. Murray, *Langmuir*, 2001, **17**, 481–488.
12 L. A. Gugliotti, D. L. Feldheim and B. E. Eaton, *Science*, 2004, **304**, 850–853; Y. Sun, L. Zhang, H. Zhou, Y. Zhu, E. Sutter, Y. Ji, M. H. Rafailovich and J. C. Sokolov, *Chem. Mater.*, 2007, **19**, 2065–2070; Q. Guo, Y. Zhao, W. L. Mao, Z. Wang, Y. Xiong and Y. Xia, *Nano Lett.*, 2008, **8**, 972–975; B. Lim, Y. Xiong and Y. Xia, *Angew. Chem., Int. Ed.*, 2007, **46**, 9279–9282; Y. Xiong and Y. Xia, *Adv. Mater.*, 2007, **19**, 3385–3391.
13 F. A. Lewis, *The Palladium/Hydrogen System*, Academic Press Inc., London, 1967.
14 L. Wang and R. T. Yang, *Energy Environ. Sci.*, 2008, **1**, 268–279.
15 C. Feng, R. Zhang, P. Yin, L. Li, L. Guo and Z. Shen, *Nanotechnology*, 2008, **19**, 305601.
16 S. Gao, H. Zhang, X. Wang, W. Mai, C. Peng and L. Ge, *Nanotechnology*, 2005, **16**, 1234–1237.
17 L. Pei, K. Mori and M. Adachi, *Langmuir*, 2004, **20**, 7837–7843; G. Ramanath, J. D'Arcy-Gall, T. Maddanimath, A. V. Ellis, P. G. Ganesan, R. Goswami, A. Kumar and K. Vijayamohanan, *Langmuir*, 2004, **20**, 5583–5587.
18 Y. Song, R. M. Garcia, R. M. Dorin, H. Wang, Y. Qiu, E. N. Coker, W. A. Steen, J. E. Miller and J. A. Shelnutt, *Nano Lett.*, 2007, **7**, 3650–3655.
19 D. Wang, H. Luo, R. Kou, M. P. Gil, S. Xiao, V. O. Golub, Z. Yang, C. J. Brinker and Y. Lu, *Angew. Chem., Int. Ed.*, 2004, **43**, 6169–6173.
20 S. Wang, X. Wang and S. P. Jiang, *Nanotechnology*, 2008, **19**, 455602.
21 R. L. Brutchey and D. E. Morse, *Chem. Rev.*, 2008, **108**, 4915–4934.
22 R. R. Naik, S. J. Stringer, G. Argarwal, S. E. Jones and M. O. Stone, *Nat. Mater.*, 2002, **1**, 169–172.
23 S.-W. Lee, C. Mao, C. E. Flynn and A. M. Belcher, *Science*, 2002, **296**, 892–895.
24 S. R. Whaley, D. S. English, E. L. Hu, P. F. Barbara and A. M. Belcher, *Nature*, 2000, **405**, 665–668.
25 B. D. Reiss, C. Mao, D. J. Solis, K. S. Ryan, T. Thomson and A. M. Belcher, *Nano Lett.*, 2004, **4**, 1127–1132.
26 G. Ahmad, M. B. Dickerson, Y. Cai, S. E. Jones, E. M. Ernst, J. P. Vernon, M. S. Haluska, Y. Fang, J. Wang, G. Subramanyam, R. R. Naik and K. H. Sandhage, *J. Am. Chem. Soc.*, 2008, **130**, 4–5.
27 M. B. Dickerson, S. E. Jones, Y. Cai, G. Ahmad, R. R. Naik, N. Kroger and K. H. Sandhage, *Chem. Mater.*, 2008, **20**, 1578–1584.
28 J. L. Sumerel, W. Yang, D. Kisailus, J. C. Weaver, J. H. Choi and D. E. Morse, *Chem. Mater.*, 2003, **15**, 4804–4809.
29 D. Kisailus, J. H. Choi, J. C. Weaver, W. Yang and D. E. Morse, *Adv. Mater.*, 2005, **17**, 314–318.
30 N. Kröger, R. Deutzmann and M. Sumper, *Science*, 1999, **286**, 1129–1132.
31 M. R. Knecht and D. W. Wright, *Chem. Commun.*, 2003, 3038–3039.
32 S. L. Sewell and D. W. Wright, *Chem. Mater.*, 2006, **18**, 3108–3113.
33 K. E. Cole, A. N. Ortiz, M. A. Schoonen and A. M. Valentine, *Chem. Mater.*, 2006, **18**, 4592–4599.
34 *Fmoc Solid Phase Peptide Synthesis: A Practical Approach*, ed. W. C. Chan and P. D. White, Oxford University Press, New York, 2003.
35 R. W. J. Scott, O. M. Wilson and R. M. Crooks, *J. Phys. Chem. B*, 2005, **109**, 692–704.
36 R. W. J. Scott, H. Ye, R. R. Henriquez and R. M. Crooks, *Chem. Mater.*, 2003, **15**, 3873–3878.
37 J. A. Creighton and D. G. Eadon, *J. Chem. Soc., Faraday Trans.*, 1991, **87**, 3881–3891.
38 J. M. Slocik, M. O. Stone and R. R. Naik, *Small*, 2005, **1**, 1048–1052.
39 R. B. Pandey, H. Heinz, B. L. Farmer, J. M. Slocik, R. R. Naik and L. F. Drummy, *Phys. Chem. Chem. Phys.*, 2009, **11**, 1989–2001.
40 P. Espinet and A. M. Echavarren, *Angew. Chem., Int. Ed.*, 2004, **43**, 4704–4734; J. K. Stille, *Angew. Chem., Int. Ed. Engl.*, 1986, **25**, 508–524.
41 Y. Niu, L. K. Yeung and R. M. Crooks, *J. Am. Chem. Soc.*, 2001, **123**, 6840–6846; T. Ueno, M. Suzuki, T. Goto, T. Matsumoto, K. Nagayama and Y. Watanabe, *Angew. Chem., Int. Ed.*, 2004, **43**, 2527–2530.
42 G. Smith, C. J. Ackerson, K. J. Baustian and D. L. Feldheim, *J. Mater. Chem.*, 2009, **19**, 8299–8306.